Transiting Exoplanet Monitoring Project (TEMP). V. Transit Follow Up for HAT-P-9b, HAT-P-32b, and HAT-P-36b

Yong-Hao Wang[1,2], Songhu Wang[3,12], Tobias C. Hinse[4,5], Zhen-Yu Wu[1,2], Allen B. Davis[3], Yasunori Hori[6,7], Joh-Na Yoon[8], Wonyong Han[9], Jun-Dan Nie[1], Hui-Gen Liu[10], Hui Zhang[10], Ji-Lin Zhou[10], R. A. Wittenmyer[11], Xi-Yan Peng[1], and Gregory Laughlin[3]

[1] Key Laboratory of Optical Astronomy, National Astronomical Observatories, Chinese Academy of Sciences, Beijing 100012, People's Republic of China [2] School of Astronomy and Space Science, University of Chinese Academy of Sciences, Beijing 101408, People's Republic of China [3] Department of Astronomy, Yale University, New Haven, CT 06511, USA; song-hu.wang@yale.edu [4] Department of Astronomy and Space Science, Chungnam National University, 34134 Daejeon, Republic of Korea [5] Korea Astronomy & Space Science Institute, 34055 Daejeon, Republic of Korea [6] National Astronomical Observatory of Japan, NINS, 2-21-1 Osawa, Mitaka, Tokyo 181-8588, Japan [7] Astrobiology Center, 2-21-1 Osawa, Mitaka, Tokyo, 181-8588, Japan [8] Chungbuk National University Observatory, 361-763 Cheongju, Republic of Korea [9] Korea Astronomy & Space Science Institute, 305-348 Daejeon, Republic of Korea [10] School of Astronomy and Space Science and Key Laboratory of Modern Astronomy and Astrophysics in Ministry of Education, Nanjing University, Nanjing 210093, People's Republic of China [11] University of Southern Queensland, Centre for Astrophysics, Toowoomba, Queensland 4350, Australia

Abstract

During the past five years, 6, 7, and 26 transit observations were carried out for the HAT-P-9b, HAT-P-32b, and HAT-P-36b systems, respectively, through the Transiting Exoplanet Monitoring Project network. Combined with the published photometric data and radial-velocity measurements, our new photometry allows us to revisit the system parameters and search for additional close-in planetary companions in these hot Jupiter systems. We measure an updated $R_P/R_* = 0.1260 \pm 0.0011$ for HAT-P-36 system in the R band, which is 4.5σ larger than the published i-band radius ratio of 0.1186 ± 0.0012. We also perform a transit timing variation (TTV) analysis for each system. Because no significant TTVs were found, we place an upper mass limit on an additional planet for each system.

Key words: planets and satellites: fundamental parameters – stars: fundamental parameters – techniques: photometric

1. Introduction

Long-term high-precision transit follow-up observations allow us to refine planetary parameters (Holman et al. 2006; Southworth et al. 2009; Hoyer et al. 2012; Wang et al. 2017b) and orbital ephemerides (Wang et al. 2018c), which are vital for future transit-related studies, such as transmission spectra observations (Bean et al. 2010) and Rossiter–McLaughlin (RM) effect measurements (Winn & Fabrycky 2015; Wang et al. 2018a).

Moreover, these observations allow us to perform transit timing variation (TTV) analyses to detect additional close-in planetary companions in known hot Jupiter systems (Agol et al. 2005; Holman & Murray 2005). The absence

or presence of such close-in companions is the key to distinguishing the competing formation mechanisms for producing hot Jupiters (Millholland et al. 2016; Wang et al. 2018b). Although great efforts had been devoted to searching for additional companions in hot Jupiter systems (e.g., TLCP, Holman et al. 2006; TraMoS, Hoyer et al. 2012; TASTE, Nascimbeni et al. 2011; YETI, Raetz et al. 2015; TRAPPIST, Gillon et al. 2012; HoSTS, Gómez Maqueo Chew et al. 2013; and Friends of Hot Jupiters, Knutson et al. 2014), no convincing detection has been reported. Two additional close-in planets, however, were detected in the WASP-47 system (Becker et al. 2015) by the *Kepler* spacecraft during its *K*2 mission, which implies that hot Jupiters may not as lonely as we thought (Steffen et al. 2012; Huang et al. 2016).

To further constrain the occurrence rate of close-in companions to hot Jupiters, as well as to refine the transit parameters for known exoplanet systems, we initiated the Transiting Exoplanet Monitoring Project (TEMP) to perform a homogeneous study for a large sample of transiting exoplanets based on long-term high-precision follow-up observations. Most of the planets observed by TEMP are hot Jupiters detected by ground-based transit surveys, such as SuperWASP (Pollacco et al. 2006), HATNet (Bakos et al. 2004), HATSouth (Bakos et al. 2013), KELT (Pepper et al. 2007), and CSTAR (Wang et al. 2014), which usually give photometric observations that are limited in quality or quantity. For more details about TEMP we refer the reader to Wang et al. (2018b).

In this paper, we present refined system parameters, updated orbital ephemerides, and TTV analyses for the HAT-P-9b, HAT-P-32b, and HAT-P-36b systems based on our 39 new light curves in conjunction with the published photometric and velocimetric data.

HAT-P-9b was discovered by Shporer et al. (2009a), who reported a hot Jupiter (M_P = 0.78 M_J, R_P = 1.40 R_J) transiting a moderately faint late F-star (M_* = 1.28 $M_\odot$, R_* = 1.32 $R_\odot$) with an orbital period of 3.92 days. Four light curves were presented in their paper. In this work we present six more light curves.

HAT-P-32b was detected by Hartman et al. (2011), who argued that the planet is a highly inflated hot Jupiter (M_P =0.94 M_J, R_P = 2.04 R_J) transiting a late F/ early G dwarf star (M_* = 1.18 $M_\odot$, R_* = 1.39 $R_\odot$) with an orbital period of 2.15 days. Five light curves were presented in their paper. Seven new light curves are presented in this work.

HAT-P-36b was found by Bakos et al. (2012), who announced a hot Jupiter (M_P = 1.83 M_J, R_P = 1.26 R_J) transiting a Sun-like star (M_* = 1.02 $M_\odot$, R_* = 1.10 $R_\odot$) with an orbital period of 1.33 days. Four light curves were presented in their work, but only one of which records a complete transit. In this work, we present 26 new light curves, 17 of which are complete transits.

We organize this paper as follows. In Section 2, we present detailed descriptions of the transit observations and data reduction. We describe the light curve analyses in Section 3. In Section 4, we present our results and

discuss their implications. In Section 5, we present a brief summary of this work.

2. Observations and Data Reduction

2.1. Photometric Observations

A total of six light curves were obtained for the HAT-P-9b system between 2016 January and 2017 February using the Xinglong Schmidt Telescope and Xinglong 60 cm Telescope operated by the National Astronomical Observatories of China. Seven light curves were obtained for the HAT-P-32b system between 2012 November and 2016 January using the same two telescopes. For the HAT-P-36b system, we collected a total of 26 light curves using the aforementioned telescopes as well as the Chungbuk National University Observatory in Jincheon (CbNUO) 60 cm Telescope (Kim et al. 2014), which is operated by CbNUOJ in South Korea. The observations of the HAT-P-36b system span about six years from 2012 March to 2017 April.

The Xinglong Schmidt Telescope (Zhou et al. 1999, 2001) is equipped with a 4K × 4K charge-coupled device (CCD). The field of view (FOV) is 94' × 94', and the pixel scale is $1\farcs38$ pixel^{-1}. The images were windowed down to 512 × 512 pixels to reduce the readout time from 93 s to 12 s. A Johnson/Cousins *R*-band filter was used for this telescope during our observations.

The Xinglong 60 cm Telescope used three different CCDs over the course of our observing program. Before 2014 November, the telescope was equipped with a 512 × 512 CCD, with a FOV of 17' × 17', a pixel scale of $1\farcs95$ pixel^{-1}, and a standard readout time of 3 s. After that, the telescope used a 1K × 1K CCD, giving a FOV of 17' × 17', a pixel scale of $0\farcs99$ pixel^{-1}, and a readout time of about 23 s. In 2015 October readout problems led to this CCD being replaced by a 2K × 2K CCD with a FOV of 36' × 36', a pixel scale of $1\farcs06$ pixel^{-1}, and a readout time of 6 s. Finally in 2016 June the 1K × 1K CCD was equipped again and used for the rest of the observing program. All of the observations for this telescope also used a Johnson/Cousins *R*-band filter.

The CCD system of the CbNUO 60 cm Telescope was upgraded in 2012/2013. For the 2012 observations, a 1530 × 1020 SBIG ST-8XE CCD was used, giving a FOV of 27' × 18', a pixel scale of $1\farcs05$ pixel^{-1}, and a readout time of 10 s. The 2013 observations used a 4K × 4K SBIG STX-16083 CCD, which had a FOV of 72' × 72', a pixel scale of $1\farcs05$ pixel^{-1}, and a readout time of 18 s. The 2012 observations were taken with no filter, and the 2013 observations used an *R*-band filter.

In order to increase the duty cycle of the observations, and reduce the Poisson and scintillation noise, we slightly defocused each telescope following the description in Southworth et al. (2009) and Hinse et al. (2015). The exposure time was set based on the target magnitude and weather conditions to get ideal cadence and enough counts in the CCD linear response regime. Exposure times would be adjusted due to significant weather variations, but we kept it constant during the ingress and egress

phases, as it is important for accurate determination of mid-transit times. The telescope times were frequently updated based on GPS time servers. For each exposure, the beginning time was recorded in the image header using the UTC time standard. The summaries of our observations for the HAT-P-9b, HAT-P-32b, and HAT-P-36b systems are listed in Tables 1, 2, and 3, respectively.

Table 1
Overview of Observations and Data Reduction for HAT-P-9

Date (UTC)	Time (UTC)	Telescope	Band	Frames	Exposure (s)	Read (s)	Air Mass	Moon Illum.	Comp. Stars	Aperture[a] (pixels)	Scatter[b] (mmag)
2016 Jan 11	15: 38: 45 → 22: 02: 56	Xinglong 60 cm	*R*	472	35–50	13	1.01 → 1.00 → 2.45	0.03	4	18	2.3
2016 Mar 10	11: 09: 20 → 16: 19: 25	Xinglong Schmidt	*R*	275	45–60	12	1.03 → 1.00 → 1.46	0.04	4	10	2.5
2016 Nov 08	16: 10: 50 → 21: 53: 45	Xinglong Schmidt	*R*	135	130–150	12	1.47 → 1.00 → 1.06	0.59	4	12	1.8
2016 Dec 29	16: 43: 02 → 21: 34: 39	Xinglong Schmidt	*R*	133	120	12	1.00 → 1.66	0.00	4	14	1.5
2017 Jan 06	12: 28: 55 → 17: 31: 00	Xinglong Schmidt	*R*	112	120–180	12	1.43 → 1.00 → 1.03	0.60	3	10	2.2
2017 Feb 26	11: 39: 06 → 17: 35: 08	Xinglong Schmidt	*R*	138	140–160	12	1.05 → 1.00 → 1.62	0.00	4	14	2.0

Notes.
[a] This column indicates the aperture diameter used in SExtractor.
[b] This column presents the rms scatter of residuals from the best-fitting model.

Table 2
Overview of Observations and Data Reduction for HAT-P-32

Date (UTC)	Time (UTC)	Telescope	Band	Frames	Exposure (s)	Read (s)	Air Mass	Moon Illum.	Comp. Stars	Aperture[a] (pixels)	Scatter[b] (mmag)
2012 Nov 05	12:02:32 → 19:28:02	Xinglong Schmidt	*R*	312	30–50	12	1.21 → 1.01 → 1.43	0.63	5	17	1.9
2012 Nov 18	11:30:17 → 17:07:22	Xinglong Schmidt	*R*	236	35	12	1.17 → 1.01 → 1.16	0.30	3	17	3.3
2012 Dec 03	12:59:24 → 17:57:58	Xinglong Schmidt	*R*	226	30	12	1.01 → 1.51	0.78	4	17	2.0
2013 Dec 10	12:10:40 → 16:59:22	Xinglong Schmidt	*R*	173	60	12	1.02 → 1.01 → 1.39	0.62	5	13	2.0
2014 Dec 17	11:23:21 → 16:08:56	Xinglong Schmidt	*R*	336	30–40	12	1.03 → 1.01 → 1.29	0.21	3	18	2.7
2015 Jan 01	11:58:10 → 16:27:07	Xinglong Schmidt	*R*	273	40–60	12	1.01 → 1.63	0.88	4	13	3.2
2016 Jan 08	10:27:14 → 15:29:50	Xinglong 60 cm	*R*	552	25–30	13	1.01 → 1.46	0.02	4	20	1.9

Notes.
[a] This column indicates the aperture diameter used in SExtractor.
[b] This column presents the rms scatter of residuals from the best-fitting model.

Table 3
Overview of Observations and Data Reduction for HAT-P-36

Date (UTC)	Time (UTC)	Telescope	Band	Frames	Exposure (s)	Read (s)	Air Mass	Moon Illum.	Comp. Stars	Aperture[a] (pixels)	Scatter[b] (mmag)
2012 Mar 20	13:25:51 → 19:50:38	CbNUO 60 cm	*N*[c]	179	120	10	1.17→1.00→1.34	0.04	5	16	1.8
2012 Mar 28	13:07:46 → 19:01:14	CbNUO 60 cm	*N*[c]	163	120	10	1.15→1.00→1.28	0.30	5	18	1.8
2013 Mar 04	14:09:40 → 20:47:21	CbNUO 60 cm	*R*	175	120	18	1.22 → 1.00 → 1.32	0.53	3	15	2.2
2013 Mar 20	13:26:42 → 19:58:27	CbNUO 60 cm	*R*	91	240	18	1.17 → 1.00 → 1.38	0.59	5	15	1.2
2014 Mar 04	16:32:07 → 21:50:59	Xinglong 60 cm	*R*	274	60	3	1.04 → 1.00 → 1.37	0.15	3	16	3.4
2014 Mar 08	15:48:53 → 21:54:47	Xinglong 60 cm	*R*	344	60	3	1.07 → 1.00 → 1.45	0.52	3	12	3.4
2014 Mar 12	15:32:33 → 21:49:45	Xinglong 60 cm	*R*	307	60–90	3	1.07 → 1.00 → 1.50	0.86	3	9	4.1
2014 Apr 01	11:40:47 → 21:05:00	Xinglong 60 cm	*R*	460	90	3	1.47 → 1.00 → 1.69	0.05	3	8	4.6
2014 Apr 05	11:41:21 → 21:02:57	Xinglong 60 cm	*R*	463	60–80	3	1.40 → 1.00 → 1.79	0.35	3	8	3.2
2014 May 07	12:07:56 → 19:15:03	Xinglong 60 cm	*R*	385	60	3	1.05 → 1.00 → 1.93	0.56	3	8	4.4
2015 Feb 04	16:50:42 → 22:17:22	Xinglong 60 cm	*R*	238	60	23	1.18 → 1.00 → 1.14	0.99	4	12	3.1
2015 Feb 12	17:11:42 → 22:20:31	Xinglong 60 cm	*R*	225	60	23	1.08 → 1.00 → 1.21	0.44	3	17	2.6
2015 Feb 16	16:56:47 → 22:12:53	Xinglong 60 cm	*R*	230	60	23	1.08 → 1.00 → 1.23	0.08	3	17	2.3
2015 Apr 25	11:58:38 → 19:38:56	Xinglong 60 cm	*R*	335	60	23	1.13 → 1.00 → 1.75	0.47	3	12	2.8
2016 Jan 10	16:23:35 → 22:43:20	Xinglong 60 cm	*R*	559	35	6	1.68 → 1.00 → 1.04	0.01	3	18	2.9
2016 Jan 14	15:41:41 → 20:18:11	Xinglong 60 cm	*R*	299	50	6	1.87 → 1.02	0.25	4	16	2.6
2016 Jan 18	15:26:35 → 19:12:18	Xinglong 60 cm	*R*	88	150	6	1.86 → 1.06	0.69	3	25	3.1
2016 Feb 15	13:37:47 → 16:23:57	Xinglong 60 cm	*R*	65	150	6	1.85 → 1.15	0.54	3	26	2.7
2016 Feb 16	18:09:38 → 22:03:27	Xinglong Schmidt	*R*	80	180	12	1.02 → 1.00 → 1.21	0.65	3	14	2.7
2016 Feb 20	17:44:32 → 21:58:28	Xinglong Schmidt	*R*	108	140	12	1.02 → 1.00 → 1.24	0.96	3	13	2.6
2016 Feb 28	17:52:14 → 21:51:40	Xinglong Schmidt	*R*	75	180	12	1.00 → 1.30	0.71	3	15	2.0
2016 Mar 11	16:53:28 → 21:39:41	Xinglong 60 cm	*R*	675	20	6	1.01 → 1.00 → 1.45	0.10	5	20	3.6
2016 Apr 12	14:24:58 → 17:19:11	Xinglong 60 cm	*R*	226	30	6	1.05 → 1.00 → 1.04	0.29	3	12	3.3
2016 May 06	13:34:20 → 16:24:43	Xinglong 60 cm	*R*	221	40	6	1.00 → 1.15	0.00	3	15	5.3
2016 Jun 24	12:39:30 → 16:24:16	Xinglong 60 cm	*R*	258	25–30	23	1.10 → 2.13	0.81	3	15	6.3
2017 Apr 20	13:39:23 → 17:00:24	Xinglong 60 cm	*R*	263	20	23	1.03 → 1.00 → 1.10	0.37	3	14	5.4

Notes.
[a] This column indicates the aperture diameter used in SExtractor.
[b] This column presents the rms scatter of residuals from the best-fitting model.
[c] No band, empty band wheel slot.

2.2. Data Reduction

We perform a TEMP data reduction with a homogeneous routine to avoid adding systematic errors. The basic reduction procedure is described in

Wang et al. (2017b). There is no exception in this work, so we will not repeat the reduction details for each system, only give a brief description for all of the three systems as follows.

The raw science frames were homogeneously calibrated using a standard procedure including bias and flat corrections. Aperture differential photometry was performed with SExtractor (Bertin & Arnouts 1996). Reference stars were chosen based on a photometric non-variability test. Aperture diameters from 5 to 35 pixels were manually varied to get the best differential light curves. Linear trends caused by variations in weather conditions were removed, and the time stamps were converted from UTC to BJD_{TDB} following Eastman et al. (2010). The number of comparison stars used and the aperture sizes for each observation for HAT-P-9b, HAT-P-32b, and HAT-P-36b are given in Tables 1, 2, and 3. The final light curves are presented in Tables 4, 5, and 6, respectively.

Table 4
Photometry of HAT-P-9

BJD_{TDB}	Relative Flux	Scatter	Telescope	Band
2457399.158375	0.9984	0.0027	Xinglong 60 cm	*R*
2457399.158845	0.9971	0.0027	Xinglong 60 cm	*R*
2457399.159315	0.9971	0.0027	Xinglong 60 cm	*R*
2457399.159784	0.9956	0.0027	Xinglong 60 cm	*R*
2457399.160722	0.9953	0.0027	Xinglong 60 cm	*R*
2457399.161663	0.9972	0.0027	Xinglong 60 cm	*R*
2457399.162132	1.0032	0.0027	Xinglong 60 cm	*R*
2457399.162632	0.9971	0.0027	Xinglong 60 cm	*R*
2457399.163160	0.9981	0.0027	Xinglong 60 cm	*R*
2457399.163689	0.9999	0.0027	Xinglong 60 cm	*R*
2457399.164217	0.9978	0.0027	Xinglong 60 cm	*R*
2457399.164744	1.0008	0.0027	Xinglong 60 cm	*R*
2457399.165271	0.9970	0.0027	Xinglong 60 cm	*R*
2457399.165800	0.9976	0.0027	Xinglong 60 cm	*R*
2457399.166854	1.0027	0.0027	Xinglong 60 cm	*R*
2457399.167381	0.9994	0.0027	Xinglong 60 cm	*R*

(This table is available in its entirety in machine-readable form.)

Table 5
Photometry of HAT-P-32

BJD_{TDB}	Relative Flux	Scatter	Telescope	Band
2456237.058708	1.0000	0.0020	Xinglong Schmidt	*R*
2456237.059669	0.9982	0.0020	Xinglong Schmidt	*R*
2456237.060630	0.9963	0.0020	Xinglong Schmidt	*R*
2456237.061602	1.0018	0.0020	Xinglong Schmidt	*R*
2456237.065051	0.9991	0.0020	Xinglong Schmidt	*R*
2456237.065942	0.9991	0.0020	Xinglong Schmidt	*R*
2456237.066856	0.9982	0.0020	Xinglong Schmidt	*R*
2456237.067771	1.0018	0.0020	Xinglong Schmidt	*R*
2456237.068639	0.9991	0.0020	Xinglong Schmidt	*R*
2456237.069565	0.9991	0.0020	Xinglong Schmidt	*R*
2456237.070479	0.9963	0.0020	Xinglong Schmidt	*R*
2456237.071440	1.0009	0.0020	Xinglong Schmidt	*R*
2456237.072354	0.9972	0.0020	Xinglong Schmidt	*R*
2456237.073257	0.9972	0.0020	Xinglong Schmidt	*R*
2456237.074171	1.0009	0.0020	Xinglong Schmidt	*R*
2456237.075074	1.0000	0.0020	Xinglong Schmidt	*R*

(This table is available in its entirety in machine-readable form.)

Table 6
Photometry of HAT-P-36

BJD_{TDB}	Relative Flux	Scatter	Telescope	Band[a]
2456007.065117	1.0020	0.0022	CbNUO 60 cm	*N*
2456007.066610	0.9972	0.0022	CbNUO 60 cm	*N*
2456007.068103	0.9973	0.0022	CbNUO 60 cm	*N*
2456007.069596	0.9998	0.0022	CbNUO 60 cm	*N*
2456007.071100	1.0010	0.0022	CbNUO 60 cm	*N*
2456007.072605	0.9950	0.0022	CbNUO 60 cm	*N*
2456007.074098	1.0010	0.0022	CbNUO 60 cm	*N*
2456007.075626	0.9974	0.0022	CbNUO 60 cm	*N*
2456007.077107	1.0003	0.0022	CbNUO 60 cm	*N*
2456007.078600	0.9968	0.0022	CbNUO 60 cm	*N*
2456007.080093	1.0030	0.0022	CbNUO 60 cm	*N*
2456007.081586	1.0024	0.0022	CbNUO 60 cm	*N*
2456007.083079	1.0024	0.0022	CbNUO 60 cm	*N*
2456007.084584	1.0002	0.0022	CbNUO 60 cm	*N*
2456007.086112	0.9981	0.0022	CbNUO 60 cm	*N*
2456007.087605	0.9992	0.0022	CbNUO 60 cm	*N*

Note.
[a] *N* band means that there is no band during these observations.

(This table is available in its entirety in machine-readable form.)

3. Data Analyses

3.1. Global Fits for System Parameters

To refine the system parameters for these three systems, we performed global fits on our new light curves together with published radial-velocity (RV) data using a fast exoplanetary fitting package EXOFAST.[13] The package calculates the parameter uncertainties through a differential evolution Markov chain Monte Carlo (DE-MCMC) algorithm. See Eastman et al. (2013) for more details about EXOFAST.

The basic processes of these global fits were similar to that described in Wang et al. (2017b). The RV data we used were from Shporer et al. (2009a), Knutson et al. (2014), and Bakos et al. (2012) for the HAT-P-9b, HAT-P-32b, and HAT-P-36b systems, respectively. The light curves we used in the global fits were from our data. We only use those with an rms scatter less than 2.5 mmag. The priors for system parameters in the fits were drawn from Shporer et al. (2009a), Hartman et al. (2011), and Bakos et al. (2012) for the HAT-P-9b, HAT-P-32b, and HAT-P-36b systems, respectively. The priors for the limb-darkening parameters (the linear limb-darkening coefficient u_1 and the quadratic limb-darkening coefficient u_2) for each system were obtained from Claret & Bloemen (2011). During the fits, the limb-darkening parameters and stellar parameters (effective temperature $T_{\rm eff}$, metalicity $[{\rm Fe/H}]$, and surface gravity $\log(g_*)$) were kept fixed and the remaining parameters were set to be freely varied.

In the first stage of the global fit, EXOFAST fit the RV and transit data independently to scale the uncertainties with a reduced $\chi^2_{\rm red} = 1$ for each best-fitting model. Then it fits both data sets simultaneously with 32 Markov chains. The solution converged when the Gelman–Rubin statistic was below 1.01 and the number of independent draws exceeded 1000 (Eastman et al. 2013). EXOFAST stopped after passing the convergence test six times. The resulting system parameters and their 1σ credible uncertainties for each system are listed in Tables 7–9.

Table 7
System Parameters for HAT-P-9

Parameter	Units	This Work	Shporer et al. (2009a)	Southworth (2012)
Stellar Parameters:				
M_*	Mass ($M_\odot$)	$1.281^{+0.057}_{-0.056}$	1.28 ± 0.13	1.28 ± 0.10
R_*	Radius ($R_\odot$)	$1.338^{+0.065}_{-0.060}$	1.32 ± 0.07	1.339 ± 0.08
L_*	Luminosity ($L_\odot$)	$2.62^{+0.26}_{-0.23}$	...	...
ρ_*	Density (cgs)	$0.755^{+0.094}_{-0.088}$	...	...
$\log(g_*)$	Surface gravity (cgs)	$4.293^{+0.033}_{-0.035}$ [a]	$4.29^{+0.03}_{-0.04}$	4.293 ± 0.046
$T_{\rm eff}$	Effective temperature (K)	6350 ± 150 [a]	6350 ± 150	...
[Fe/H]	Metalicity	0.12 ± 0.20 [a]	0.12 ± 0.20	...
Planetary Parameters:				
e	Eccentricity	$0.084^{+0.052}_{-0.047}$	...	...
ω_*	Argument of periastron (degrees)	152^{+42}_{-39}	...	...
P	Period (days)	$3.92281072 \pm 0.00000102$ [b]	3.92289 ± 0.00004	3.922814 ± 0.000002
a	Semimajor axis (au)	0.05287 ± 0.00078	0.053 ± 0.002	0.0529 ± 0.0014
M_P	Mass (M_J)	$0.749^{+0.064}_{-0.063}$	0.78 ± 0.09	0.778 ± 0.083
R_P	Radius (R_J)	$1.393^{+0.067}_{-0.065}$	1.40 ± 0.06	1.38 ± 0.10
ρ_P	Density (cgs)	$0.342^{+0.057}_{-0.048}$	0.35 ± 0.06	...
$\log(g_P)$	Surface gravity	$2.979^{+0.050}_{-0.051}$	...	...
$T_{\rm eq}$	Equilibrium temperature (K)	1540^{+32}_{-30}	1530 ± 40	1540 ± 53
Θ	Safronov number	$0.0443^{+0.0042}_{-0.0040}$	0.046 ± 0.007	0.0463 ± 0.0056
$\langle F \rangle$	Incident flux (10^9 erg s^{-1} cm^{-2})	$1.267^{+0.10}_{-0.094}$	1.3 ± 0.3	...
RV Parameters:				
$e \cos \omega_*$	...	$-0.060^{+0.046}_{-0.050}$	...	...
$e \sin \omega_*$	...	$0.028^{+0.056}_{-0.041}$	...	...
T_P	Time of periastron (BJD$_{\rm TDB}$)	$2457811.72^{+0.47}_{-0.37}$	...	...
K	RV semi-amplitude (m s^{-1})	$82.1^{+6.5}_{-6.4}$	84.7 ± 7.9	...
$M_P \sin i$	Minimum mass (M_J)	0.748 ± 0.063	...	...
M_P / M_*	Mass ratio	$0.000558^{+0.000045}_{-0.000044}$	...	...
γ	Systemic velocity (m s^{-1})	$22666.2^{+5.4}_{-5.3}$	22665.0 ± 6.0	...
$\dot{\gamma}$	RV slope (m s^{-1} day^{-1})	$-0.047^{+0.048}_{-0.050}$	...	...
Primary Transit Parameters:				
T_C	Time of transit (BJD$_{\rm TDB}$)	$2455484.913088 \pm 0.000386$ [b]	...	...
R_P / R_*	Radius of planet in stellar radii	$0.10696^{+0.00086}_{-0.00087}$	0.1083 ± 0.0005	...
a / R_*	Semimajor axis in stellar radii	$8.50^{+0.34}_{-0.35}$	8.6 ± 0.2	...
u_1	linear limb-darkening coeff.	0.286 [c]	...	...
u_2	quadratic limb-darkening coeff.	0.320 [c]	...	...
i	Inclination (degrees)	$86.44^{+0.37}_{-0.36}$	86.5 ± 0.2	86.10 ± 0.54
b	Impact parameter	$0.510^{+0.044}_{-0.052}$	0.52 ± 0.03	...
δ	Transit depth	$0.01144^{+0.00018}_{-0.00019}$	...	...
$T_{\rm FWHM}$	FWHM duration (days)	$0.12212^{+0.00067}_{-0.00068}$	...	...
τ	Ingress/egress duration (days)	0.0178 ± 0.0013	0.019 ± 0.003	...
T_{14}	Total duration (days)	0.1400 ± 0.0014	0.143 ± 0.004	...
P_T	A priori non-grazing transit prob.	$0.1086^{+0.011}_{-0.0079}$	...	...
$P_{T,\,G}$	A priori transit prob.	$0.1347^{+0.014}_{-0.0098}$	...	...
F_0	Baseline flux	0.999726 ± 0.000100	...	...
Secondary Eclipse Parameters:				
T_S	Time of eclipse (BJD$_{\rm TDB}$)	2457812.95 ± 0.12	...	...
b_S	Impact parameter	$0.540^{+0.047}_{-0.046}$	...	...
$T_{S,\,\rm FWHM}$	FWHM duration (days)	$0.1262^{+0.0091}_{-0.0061}$	...	...
τ_S	Ingress/egress duration (days)	$0.0194^{+0.0025}_{-0.0019}$	...	...
$T_{S,14}$	Total duration (days)	$0.1457^{+0.011}_{-0.0078}$	...	...
P_S	A priori non-grazing eclipse prob.	$0.1025^{+0.0033}_{-0.0031}$	...	...
$P_{S,\,G}$	A priori eclipse prob.	$0.1270^{+0.0043}_{-0.0041}$	...	...

Notes. The published system parameters of HAT-P-9 from Shporer et al. (2009a) and Dittmann et al. (2012) are presented for comparison.
[a] These stellar parameters were directly cited from the discovery work (Shporer et al. 2009a).
[b] The P and T_C were obtained from a linear fit based on all of the mid-transit times (see Section 4.2.1).
[c] The limb-darkening parameters were obtained from Claret & Bloemen (2011).

Table 8
System Parameters for HAT-P-32

Parameter	Units	This Work	Hartman et al. (2011)	Knutson et al. (2014)
Stellar Parameters:				
M_*	Mass ($M_\odot$)	$1.132^{+0.051}_{-0.050}$	$1.176^{+0.043}_{-0.070}$	...
R_*	Radius ($R_\odot$)	$1.367^{+0.031}_{-0.030}$	1.387 ± 0.067	...
L_*	Luminosity ($L_\odot$)	$2.178^{+0.099}_{-0.096}$	2.43 ± 0.30	...
ρ_*	Density (cgs)	0.625 ± 0.014	...	...
$\log(g_*)$	Surface gravity (cgs)	4.22 ± 0.04[a]	4.22 ± 0.04	...
$T_{\rm eff}$	Effective temperature (K)	6001 ± 88[a]	6001 ± 88	...
[Fe/H]	Metalicity	-0.16 ± 0.08[a]	-0.16 ± 0.08	...
Planetary Parameters:				
e	Eccentricity	$0.159^{+0.051}_{-0.028}$	0.163 ± 0.061	$0.20^{+0.19}_{-0.13}$
ω_*	Argument of periastron (degrees)	50^{+27}_{-18}	52 ± 29	58^{+28}_{-53}
P	Period (days)	$2.15000820 \pm 0.00000013$[b]	2.150009 ± 0.000001	...
a	Semimajor axis (au)	$0.03397^{+0.00051}_{-0.00050}$	$0.0344^{+0.004}_{-0.007}$	...
M_P	Mass (M_J)	$0.68^{+0.11}_{-0.10}$	0.941 ± 0.166	0.79 ± 0.15
R_P	Radius (R_J)	1.980 ± 0.045	2.037 ± 0.099	...
ρ_P	Density (cgs)	$0.108^{+0.018}_{-0.017}$	$0.14^{+0.03}_{-0.02}$	...
$\log(g_P)$	Surface gravity	$2.632^{+0.064}_{-0.072}$	2.75 ± 0.07	...
$T_{\rm eq}$	Equilibrium temperature (K)	$1835.7^{+6.8}_{-6.9}$	1888 ± 51	...
Θ	Safronov number	$0.0205^{+0.0033}_{-0.0032}$	0.027 ± 0.004	...
$\langle F \rangle$	Incident flux (10^9 erg s^{-1} cm^{-2})	$2.505^{+0.042}_{-0.052}$	2.86 ± 0.31	...
RV Parameters:				
$e \cos \omega_*$	...	$0.101^{+0.077}_{-0.072}$	0.099 ± 0.080	$0.076^{+0.11}_{-0.079}$
$e \sin \omega_*$	...	$0.120^{+0.011}_{-0.015}$	0.124 ± 0.037	$0.15^{+0.19}_{-0.15}$
T_P	Time of periastron ($\rm BJD_{TDB}$)	$2456237.031^{+0.11}_{-0.062}$	...	...
K	RV semi-amplitude (m s^{-1})	99^{+16}_{-15}	136.1 ± 23.8	112^{+20}_{-21}
$M_P \sin i$	Minimum mass (M_J)	$0.68^{+0.11}_{-0.10}$	...	...
M_P/M_*	Mass ratio	$0.000572^{+0.000090}_{-0.000088}$	...	...
γ	Systemic velocity (m s^{-1})	76.1 ± 9.7	...	...
$\dot{\gamma}$	RV slope (m s^{-1} day^{-1})	-0.104 ± 0.015	...	-0.097 ± 0.023
Primary Transit Parameters:				
T_C	Time of transit ($\rm BJD_{TDB}$)	$2455867.402743 \pm 0.000049$[b]	$2454416.14639 \pm 0.00009$	...
R_P/R_*	Radius of planet in stellar radii	$0.14886^{+0.00056}_{-0.00054}$	0.1508 ± 0.0004	...
a/R_*	Semimajor axis in stellar radii	$5.344^{+0.040}_{-0.039}$	5.32 ± 0.22	...
u_1	linear limb-darkening coeff.	0.316[c]	...	...
u_2	quadratic limb-darkening coeff.	0.303[c]	...	...
i	Inclination (degrees)	$88.98^{+0.68}_{-0.85}$	88.7 ± 0.6	...
b	Impact parameter	$0.083^{+0.070}_{-0.055}$	$0.108^{+0.043}_{-0.044}$	...
δ	Transit depth	$0.02216^{+0.00017}_{-0.00016}$	...	...
$T_{\rm FWHM}$	FWHM duration (days)	$0.11284^{+0.00037}_{-0.00038}$	...	...
τ	Ingress/egress duration (days)	$0.01712^{+0.00032}_{-0.00015}$	0.0171 ± 0.0002	...
T_{14}	Total duration (days)	$0.13002^{+0.00052}_{-0.00049}$	0.1292 ± 0.0003	...
P_T	A priori non-grazing transit prob.	$0.1837^{+0.0037}_{-0.0036}$	...	...
$P_{T,G}$	A priori transit prob.	$0.2479^{+0.0050}_{-0.0049}$	...	...
F_0	Baseline flux	0.99940 ± 0.00013	...	...
Secondary Eclipse Parameters:				
T_S	Time of eclipse ($\rm BJD_{TDB}$)	$2456236.268^{+0.10}_{-0.098}$	2454417.357 ± 0.109	...
b_S	Impact parameter	$0.105^{+0.086}_{-0.070}$	...	...
$T_{S,\rm FWHM}$	FWHM duration (days)	$0.1431^{+0.0034}_{-0.0044}$	...	...
τ_S	Ingress/egress duration (days)	$0.02194^{+0.00047}_{-0.00055}$	0.0221 ± 0.0017	...
$T_{S,14}$	Total duration (days)	$0.1650^{+0.0038}_{-0.0048}$	0.1653 ± 0.0120	...
P_S	A priori non-grazing eclipse prob.	$0.1437^{+0.0046}_{-0.0021}$	...	...
$P_{S,G}$	A priori eclipse prob.	$0.1939^{+0.0062}_{-0.0029}$	...	...

Notes. The published system parameters of HAT-P-32 from Hartman et al. (2011) and Knutson et al. (2014) are presented for comparison.
[a] These stellar parameters were directly cited from the discovery work (Hartman et al. 2011).
[b] The P and T_C were obtained from a linear fit based on all of the mid-transit times (see Section 4.2.2).
[c] The limb-darkening parameters were obtained from Claret & Bloemen (2011).

Table 9
System Parameters for HAT-P-36

Parameter	Units	This Work	Bakos et al. (2012)	Mancini et al. (2015)
Stellar Parameters:				
M_*	Mass ($M_\odot$)	$1.049^{+0.048}_{-0.046}$	1.022 ± 0.049	1.030 ± 0.029
R_*	Radius ($R_\odot$)	$1.108^{+0.025}_{-0.024}$	1.096 ± 0.056	1.041 ± 0.013
L_*	Luminosity ($L_\odot$)	$1.053^{+0.048}_{-0.046}$	1.03 ± 0.15	...
ρ_*	Density (cgs)	$1.089^{+0.025}_{-0.024}$	...	...
$\log(g_*)$	Surface gravity (cgs)	4.37 ± 0.04[a]	4.37 ± 0.04	4.416 ± 0.010
$T_{\rm eff}$	Effective temperature (K)	5560 ± 100[a]	5560 ± 100	5620 ± 40
[Fe/H]	Metalicity	0.26 ± 0.10[a]	0.26 ± 0.10	0.25 ± 0.09
Planetary Parameters:				
e	Eccentricity	$0.063^{+0.021}_{-0.025}$	0.063 ± 0.032	...
ω_*	Argument of periastron (degrees)	51^{+20}_{-19}	95 ± 63	...
P	Period (days)	$1.32734660 \pm 0.00000033$[b]	1.327347 ± 0.000003	$1.32734683 \pm 0.00000048$
a	Semimajor axis (au)	$0.02402^{+0.00036}_{-0.00035}$	0.0238 ± 0.0004	0.02388 ± 0.00022
M_P	Mass (M_J)	$1.925^{+0.085}_{-0.081}$	1.832 ± 0.099	1.852 ± 0.088
R_P	Radius (R_J)	$1.357^{+0.035}_{-0.034}$	1.264 ± 0.071	1.304 ± 0.021
ρ_P	Density (cgs)	$0.955^{+0.057}_{-0.054}$	1.12 ± 0.19	...
$\log(g_P)$	Surface gravity	3.413 ± 0.017	3.45 ± 0.05	...
$T_{\rm eq}$	Equilibrium temperature (K)	$1820.2^{+6.7}_{-6.8}$	1823 ± 55	1788 ± 15
Θ	Safronov number	0.0649 ± 0.0026	0.067 ± 0.005	0.0658 ± 0.003
$\langle F \rangle$	Incident flux (10^9 erg s^{-1} cm^{-2})	2.479 ± 0.037	2.49 ± 0.30	...
RV Parameters:				
$e \cos \omega_*$	...	$0.037^{+0.022}_{-0.025}$	-0.002 ± 0.032	...
$e \sin \omega_*$	...	$0.045^{+0.021}_{-0.020}$	0.051 ± 0.040	...
T_P	Time of periastron (BJD$_{\rm TDB}$)	$2456698.610^{+0.065}_{-0.064}$	...	...
K	RV semi-amplitude (m s^{-1})	344 ± 11	334.7 ± 14.5	316 ± 39
$M_P \sin i$	Minimum mass (M_J)	$1.919^{+0.084}_{-0.080}$	...	...
M_P/M_*	Mass ratio	0.001754 ± 0.000061	...	...
γ	Systemic velocity (m s^{-1})	$-11.3^{+7.9}_{-7.8}$	...	...
$\dot{\gamma}$	RV slope (m s^{-1} day^{-1})	$-1.33^{+0.69}_{-0.67}$	...	...
Primary Transit Parameters:				
T_C	Time of transit (BJD$_{\rm TDB}$)	$2456698.735910 \pm 0.000149$[b]	$2455565.18144 \pm 0.00020$	$2455565.18167 \pm 0.00036$
R_P/R_*	Radius of planet in stellar radii	0.1260 ± 0.0011	0.1186 ± 0.0012	...
a/R_*	Semimajor axis in stellar radii	$4.665^{+0.035}_{-0.034}$	4.66 ± 0.22	...
u_1	linear limb-darkening coeff.	0.424[c]	...	...
u_2	quadratic limb-darkening coeff.	0.250[c]	...	...
i	Inclination (degrees)	$85.19^{+0.72}_{-0.55}$	86.0 ± 1.3	85.86 ± 0.21
b	Impact parameter	$0.373^{+0.048}_{-0.062}$	$0.312^{+0.078}_{-0.105}$	...
δ	Transit depth	$0.01588^{+0.00029}_{-0.00028}$	...	...
T_{FWHM}	FWHM duration (days)	$0.08096^{+0.00062}_{-0.00061}$	...	...
τ	Ingress/egress duration (days)	0.01205 ± 0.00062	0.0107 ± 0.0007	...
T_{14}	Total duration (days)	$0.09302^{+0.00073}_{-0.00075}$	0.0923 ± 0.0007	...
P_T	A priori non-grazing transit prob.	$0.1966^{+0.0049}_{-0.0045}$	...	...
$P_{T,\,G}$	A priori transit prob.	$0.2533^{+0.0060}_{-0.0055}$	...	...
F_0	Baseline flux	1.00022 ± 0.00012	...	...
Secondary Eclipse Parameters:				
T_S	Time of eclipse (BJD$_{\rm TDB}$)	2456698.103 ± 0.019	2455565.844 ± 0.027	...
b_S	Impact parameter	$0.408^{+0.038}_{-0.054}$	...	...
$T_{S,FWHM}$	FWHM duration (days)	$0.0871^{+0.0038}_{-0.0031}$	...	...
τ_S	Ingress/egress duration (days)	$0.01338^{+0.00034}_{-0.00032}$	0.0120 ± 0.0015	...
$T_{S,14}$	Total duration (days)	$0.1006^{+0.0036}_{-0.0031}$	0.1013 ± 0.0071	...
P_S	A priori non-grazing eclipse prob.	$0.1796^{+0.0035}_{-0.0036}$	...	...
$P_{S,\,G}$	A priori eclipse prob.	$0.2314^{+0.0048}_{-0.0049}$	...	...

Notes. The published system parameters of HAT-P-36 from Bakos et al. (2012) and Mancini et al. (2015) are presented for comparison.
[a] These stellar parameters were directly cited from the discovery work (Bakos et al. 2012).
[b] The P and T_C were obtained from a linear fit based on all of the mid-transit times (see Section 4.2.3).
[c] The limb-darkening parameters were obtained from Claret & Bloemen (2011).

3.2. Separate Fits for Mid-transit Times

To obtain precise mid-transit times with reliable uncertainties, and thus to further refine the planetary orbital ephemerides and perform TTV analyses, we separately fit each light curve using the task 9 algorithm (a residual permutation algorithm) in the JKTEBOP[14] code (Southworth et al. 2004; Southworth 2008).

The mid-transit time T_c and light scale factor F_0 were the only two free parameters in these separate fits. All of the others were fixed at the values obtained from the global fits described in Section 3.1. These fixed parameters include the sum of radii $RP/a + R_*/a$ (where R_* and RP are the absolute stellar and planetary radii, respectively, and a is the semimajor axis of the planetary orbit), ratio of the radii RP/R_*, orbital inclination i, mass ratio of the system MP/M_*, and the combination of orbital eccentricity e and periastron longitude ω_* (presented as $e\cos\omega_*$ and $e\sin\omega_*$). The limb-darkening values for each band were fixed at the values from Claret & Bloemen (2011). The mid-transit times with their 1σ credible uncertainties for each system were finally obtained and are listed in Tables 10–12.

Table 10
Mid-transit Times for HAT-P-9b

Epoch	Telescope	T_c (BJD$_{\rm TDB}$)	σ_{T_c} (s)	$O-C$ (s)
−272	Shporer et al. (2009a)	2454417.90848[a]	25.92	−6.27
−62	Dittmann et al. (2012)	2455241.69920[a]	216.00	32.55
−49	Dittmann et al. (2012)	2455292.69620[a]	77.76	72.35
488	Xinglong 60 cm	2457399.24582	120.43	95.08
503	Xinglong Schmidt	2457458.08549	104.99	−119.67
565	Xinglong Schmidt	2457701.30337	80.85	192.15
578	Xinglong Schmidt	2457752.29752	99.93	−14.40
580	Xinglong Schmidt	2457760.14058	72.42	−235.68
593	Xinglong Schmidt	2457811.14137	85.64	131.65

Note.
[a] These mid-transit times are cited directly from Shporer et al. (2009a) and Dittmann et al. (2012).

Table 11
Mid-transit Times for HAT-P-32b

Epoch	Telescope	T_c (BJD_{TDB})	σ_{T_c} (s)	$O-C$ (s)
−697	Hartman et al. (2011)	2454368.84711[a]	18.66	7.31
−684	Hartman et al. (2011)	2454396.79734[a]	32.25	18.24
−677	Hartman et al. (2011)	2454411.84695[a]	13.77	−20.75
−671	Hartman et al. (2011)	2454424.74713[a]	16.95	−9.02
−664	Hartman et al. (2011)	2454439.79714[a]	15.79	−13.82
−11	Sada et al. (2012)	2455843.75341[b]	16.42	65.43
−10	Sada et al. (2012)	2455845.90287[b]	20.74	18.06
−10	Sada et al. (2012)	2455845.90314[b]	20.74	41.39
0	Seeliger et al. (2014)	2455867.40301[b]	63.07	23.07
6	Seeliger et al. (2014)	2455880.30267[b]	28.51	−10.56
13	Seeliger et al. (2014)	2455895.35297[b]	13.82	10.40
13	Seeliger et al. (2014)	2455895.35249[b]	69.12	−31.07
14	Seeliger et al. (2014)	2455897.50328[b]	28.51	36.48
20	Seeliger et al. (2014)	2455910.40274[b]	37.15	−14.43
26	Seeliger et al. (2014)	2455923.30295[b]	26.78	−0.54
35	Seeliger et al. (2014)	2455942.65287[b]	55.30	−13.83
134	Seeliger et al. (2014)	2456155.50385[b]	22.46	0.67
135	Seeliger et al. (2014)	2456157.65470[b]	62.21	73.40
144	Gibson et al. (2013)	2456177.00392[b]	21.60	−0.37
147	Seeliger et al. (2014)	2456183.45364[b]	73.44	−26.69
147	Seeliger et al. (2014)	2456183.45361[b]	42.34	−29.28
148	Seeliger et al. (2014)	2456185.60375[b]	28.51	−17.90
160	Seeliger et al. (2014)	2456211.40361[b]	48.38	−38.50
164	Gibson et al. (2013)	2456220.00440[b]	16.42	26.92
172	Xinglong Schmidt	2456237.20386	24.84	−25.50
178	Xinglong Schmidt	2456250.10439	36.26	16.49
180	Seeliger et al. (2014)	2456254.40404[b]	19.01	−15.52
185	Xinglong Schmidt	2456265.15466	41.37	34.57
314	Seeliger et al. (2014)	2456542.50538[b]	27.65	5.27
314	Seeliger et al. (2014)	2456542.50530[b]	15.55	−1.64
314	Seeliger et al. (2014)	2456542.50522[b]	44.93	−8.55
328	Seeliger et al. (2014)	2456572.60532[b]	15.55	−9.84
340	Seeliger et al. (2014)	2456598.40539[b]	14.69	−12.29
341	Seeliger et al. (2014)	2456600.55546[b]	14.69	−6.96
354	Seeliger et al. (2014)	2456628.50585[b]	26.78	17.53
358	Xinglong Schmidt	2456637.10480	20.12	−75.62
367	Seeliger et al. (2014)	2456656.45533[b]	38.88	−36.62
531	Xinglong Schmidt	2457009.05775	69.24	56.61
538	Xinglong Schmidt	2457024.10743	39.61	23.77
711	Xinglong 60 cm Telescope	2457396.05803	78.22	−46.78

Notes.
[a] These mid-transit times are obtained from our fits based on the light curves in Hartman et al. (2011).
[b] These mid-transit times are cited directly from Sada et al. (2012), Gibson et al. (2013), and Seeliger et al. (2014).

Table 12
Mid-transit Times for HAT-P-36b

Epoch	Telescope	T_c (BJD$_{TDB}$)	σ_{T_c} (s)	$O-C$ (s)
−861	Bakos et al. (2012)	2455555.89140[a]	42.04	78.59
−830	Bakos et al. (2012)	2455597.03726[a]	86.26	−83.66
−827	Bakos et al. (2012)	2455601.02027[a]	82.48	−0.56
−821	Bakos et al. (2012)	2455608.98474[a]	85.21	33.13
−521	CbNUO 60 cm	2456007.18909	60.92	65.33
−515	CbNUO 60 cm	2456015.15110	29.65	−113.51
−258	CbNUO 60 cm	2456356.28178	90.16	111.53
−246	CbNUO 60 cm	2456372.20849	67.82	−13.24
−227	Mancini et al. (2015)	2456397.42892[a]	25.36	59.61
17	Xinglong 60 cm Telescope	2456721.30085	72.63	4.19
20	Xinglong 60 cm Telescope	2456725.28100	58.38	−159.16
23	Xinglong 60 cm Telescope	2456729.26439	82.17	−42.30
38	Xinglong 60 cm Telescope	2456749.17580	93.30	61.76
41	Xinglong 60 cm Telescope	2456753.15819	73.07	92.29
48	Mancini et al. (2015)	2456762.44829[a]	36.61	−21.81
51	Mancini et al. (2015)	2456766.43075[a]	36.58	14.13
65	Xinglong 60 cm Telescope	2456785.01425	110.19	70.05
271	Xinglong 60 cm Telescope	2457058.44614	128.65	−60.08
277	Xinglong 60 cm Telescope	2457066.41202	67.07	95.51
280	Xinglong 60 cm Telescope	2457070.39280	74.15	−13.35
331	Xinglong 60 cm Telescope	2457138.08645	63.37	−102.27
527	Xinglong 60 cm Telescope	2457398.24830	37.56	63.61
530	Xinglong 60 cm Telescope	2457402.22948	35.58	−11.22
533	Xinglong 60 cm Telescope	2457406.21179	79.67	12.21
554	Xinglong 60 cm Telescope	2457434.08580	113.94	−10.64
555	Xinglong Schmidt	2457435.41340	128.99	10.73
558	Xinglong Schmidt	2457439.39401	84.53	−112.34
564	Xinglong Schmidt	2457447.35849	45.65	−77.66
573	Xinglong 60 cm Telescope	2457459.30494	84.96	−49.05
597	Xinglong 60 cm Telescope	2457491.16331	61.79	127.44
615	Xinglong 60 cm Telescope	2457515.05405	88.24	−1.97
652	Xinglong 60 cm Telescope	2457564.16608	189.71	16.13
878	Xinglong 60 cm Telescope	2457864.14544	140.73	−68.05

Note.
[a] These mid-transit times are obtained from our fits based on the published light curves from Bakos et al. (2012) and Mancini et al. (2015).

4. Results and Discussion

4.1. System Parameters

4.1.1. HAT-P-9b

The global system parameters we obtained for the HAT-P-9 system, and those from previous studies (Shporer et al. 2009a; Southworth 2012) are listed in Table 7. The best-fitting models for the transit and RV data are plotted in Figures 1 and 2, respectively.

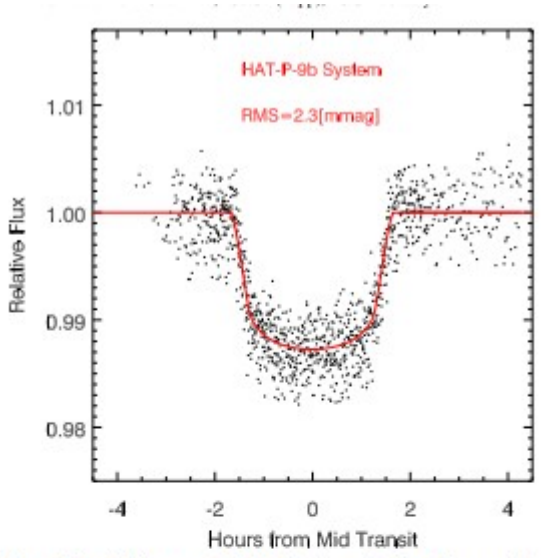

Figure 1. Phased light curve of HAT-P-9b. The resulting best-fitting model is shown by the red line, giving an rms scatter of 2.3 mmag.

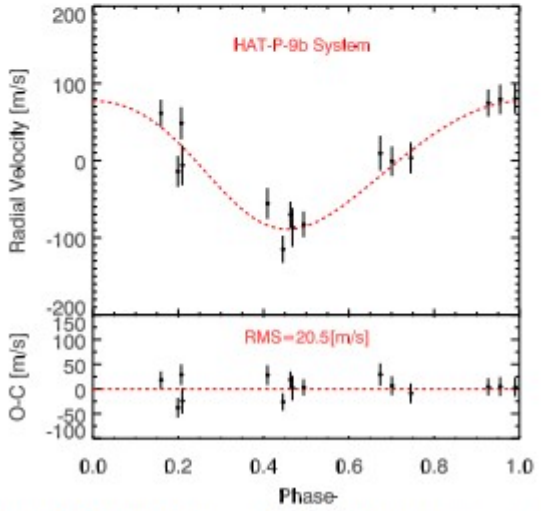

Figure 2. RV data of HAT-P-9b. Top: points with error bars are published data from Shporer et al. (2009a), and the red line is the best-fitting keplerian orbit model. Bottom: residuals plot with an rms scatter of 20.5 m s^{-1}.

As shown in Table 7, all of our new measurements of the system parameters of HAT-P-9b show excellent agreement with those in Shporer et al. (2009a) and Southworth (2012), with the high-precision light curves allowing us to place even tighter constraints on the uncertainties.

4.1.2. HAT-P-32b

The refined system parameters for the HAT-P-32b system together with those of previous studies (Hartman et al. 2011; Knutson et al. 2014) are listed in Table 8. The best-fitting models for the transit and RV data are plotted in Figures 3 and 4, respectively.

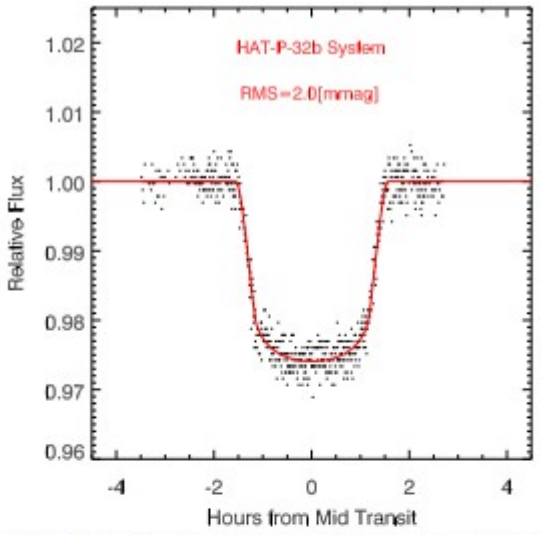

Figure 3. Phased light curve of HAT-P-32b. The resulting best-fitting model is shown by the red line, giving an rms scatter of 2.0 mmag.

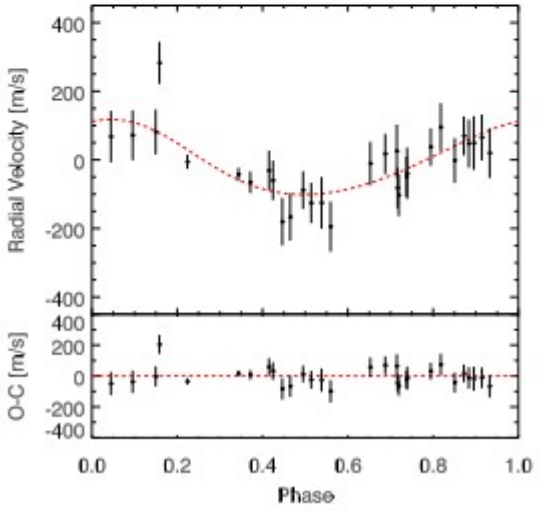

Figure 4. RV data of HAT-P-32b. Top: points with error bars are the published data from Knutson et al. (2014), and the red line is the best-fitting keplerian orbit model. Bottom: residuals plot, with an rms scatter of 62.4 m s^{-1}.

As Table 8 shows, the system parameters we found show good agreement with previous work (Hartman et al. 2011; Knutson et al. 2014).

4.1.3. HAT-P-36b

The refined system parameters resulting from our global fit for the HAT-P-36b system together with the previously published results (Bakos et al. 2012; Mancini et al. 2015) are listed in Table 9. The best-fitting models for the transit and RV data are plotted in Figures 5 and 6, respectively.

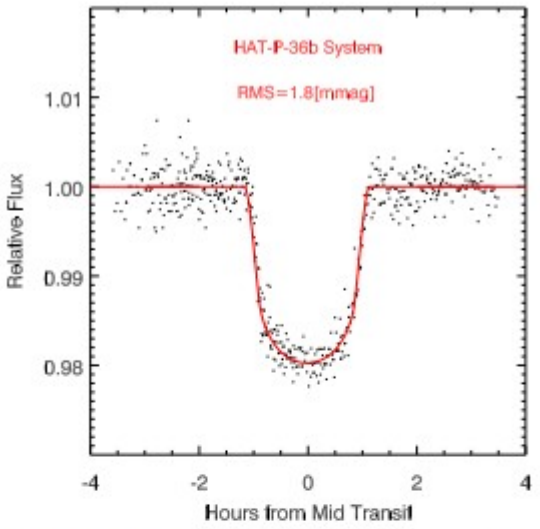

Figure 5. Phased light curve of HAT-P-36b. The resulting best-fitting model is shown by the red line, giving an rms scatter of 1.8 mmag.

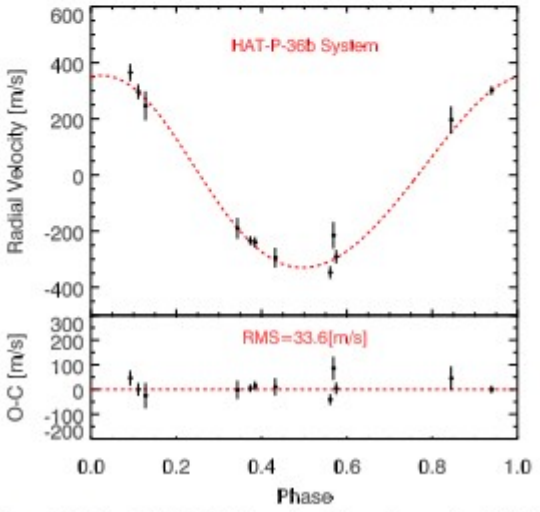

Figure 6. RV data of HAT-P-36b. Top: points with error bars are the published data from Bakos et al. (2012), and the red line is the best-fitting keplerian orbit model. Bottom: residuals plot, with an rms scatter of 33.6 m s^{-1}.

As shown in Table 9, the system parameters from our analysis show good agreement with previous studies, except for R_P/R_*. The R_P/R_* of 0.1260 ± 0.0011 we found in the R band is 4.5σ larger than the published one (0.1186 ± 0.0012) in the i band.

To demonstrate that the R_P/R_* discrepancy we found does not arise from differences in the fitting process, we conducted a fit based only on the i-band data from the discovery paper (Bakos et al. 2012). All of the resulting system parameters, including R_P/R_* (0.1192 ± 0.0010), agree with those from the discovery work. The i-band best-fitting model together with our R-band model are plotted in Figure 7 for comparison.

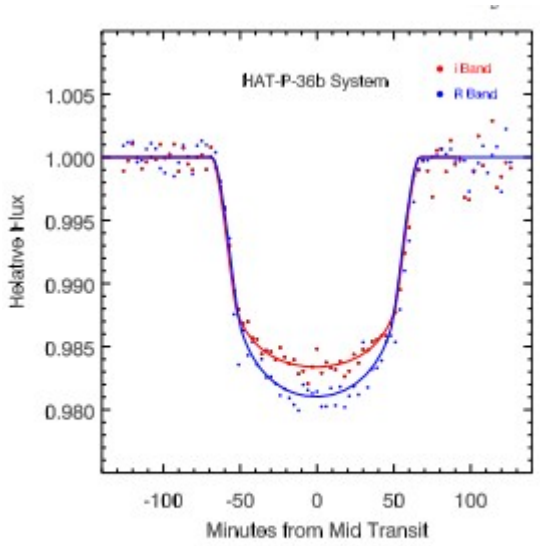

Figure 7. Phased light curves with best-fitting models of HAT-P-36b from our global fit. The red and blue lines represent the *i*-band and *R*-band data, respectively. We measure $R_P/R_* = 0.1260 \pm 0.0011$ in the *R* band, which is larger than our *i*-band value (0.1192 ± 0.0010) at the 4.6σ level.

Multi-band photometry of hot Jupiters can reveal the Rayleigh scattering and absorption features of molecules (e.g., H_2O) and metal (e.g., Na, K, TiO, VO) in their atmospheres (Sing et al. 2016). The transit-depth discrepancy we found between the *i* and *R* bands should be useful to infer atmospheric compositions and the cloud/haze properties of HAT-P-36b. The transit-depth discrepancy in different bands has also been found in previous works studying other systems (Mancini et al. 2013; Sing et al. 2015).

4.2. Mid-transit Times

4.2.1. HAT-P-9b

To perform a TTV analysis for the HAT-P-9b system, we need an accurate planetary orbital ephemeris. The orbital ephemeris in the discovery work was obtained based on four light curves within a time span of only two months (Shporer et al. 2009a). Dittmann et al. (2012) then derived a new ephemeris with two more observations, extending the time span to two years. In this work, we have added another six light curves, greatly augmenting the time span to a total of eight years.

As described in Section 3.2, we performed a separate fit for each of our six light curves to get accurate mid-transit times (T_c). The best-fitting models are plotted in Figure 8. The obtained mid-transit times together with the published ones from Shporer et al. (2009a) and Dittmann et al. (2012) are listed in Table 10. We then fit the mid-transit times with a linear function as

$$T_c(N) = T_c(0) + N \times P, \qquad (1)$$

where P is the planetary orbital period and N represents transit epoch number. $T_c(0)$ is the zero epoch mid-transit time and $T_c(N)$ is the time of epoch N. In this fit, we have chosen $T_c(0)$ to be at the middle of the data time

span, which minimized parameter correlations between $T_c(0)$ and P (Shporer et al. 2009b). The best-fitting parameters are

$$T_c(0) = 2455484.913087 \pm 0.000386\ [\mathrm{BJD_{TDB}}], \qquad (2)$$

and

$$P = 3.92281072 \pm 0.00000102\ [\mathrm{days}]. \qquad (3)$$

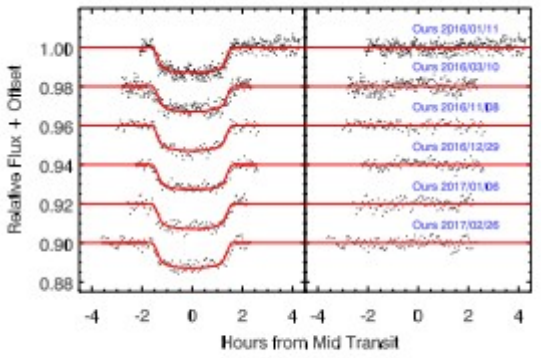

Figure 8. Six new transit light curves of HAT-P-9b. Best-fitting models are shown with red lines in the left panel, and the residuals to the fits are shown in the right.

The P from our analysis agrees with $P = 3.92289 \pm 0.00004$ found in Shporer et al. (2009a) within 2.0σ, and it agrees with $P = 3.922814 \pm 0.000002$ found in Dittmann et al. (2012) within 1.5σ. We believe our updated ephemeris is more precise and reliable due to the extended time span of the observations.

During the fitting process, the errors of the mid-transit times were rescaled to get $\chi^2/N_{\mathrm{dof}} = 1$, which provides a more conservative uncertainty for the resulting period. The uncertainties of the times presented in Table 10 as well as the error bars plotted in Figure 9, however, were not rescaled.

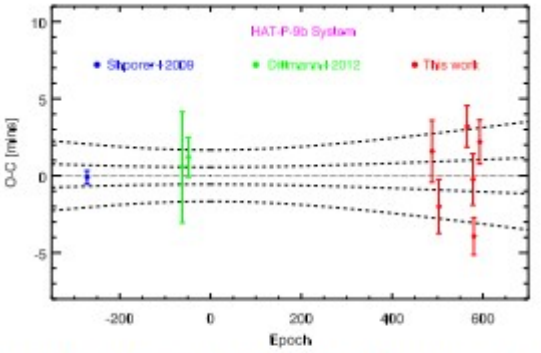

Figure 9. Transit timing variations for HAT-P-9b. The revised linear orbital ephemeris (see Equations (1)–(3)) is shown with a dotted line, with $\pm 1\sigma$ and $\pm 3\sigma$ uncertainties shown with dashed lines. The points denote residuals from the revised ephemeris; the red points represent the mid-transit times obtained from our separate fits with our photometric data, while blue and green points represent the mid-transit times cited from Shporer et al. (2009a) and Dittmann et al. (2012), respectively. All of the mid-transit times are consistent with our new ephemeris at the $\pm 3\sigma$ level, giving an rms scatter of 131 s.

Figure 9 shows the deviations of mid-transit times from our new orbital ephemeris (Equations (1)–(3)), with an rms of 131 s. Though there is no

significant TTV anomaly, we can put a upper mass limit on a potential perturber in the HAT-P-9b system (see Section 4.3).

4.2.2. HAT-P-32b

For HAT-P-32b, we used the same technique as in Section 4.2.1 to refine the orbital ephemeris and analyze TTVs. The accurate mid-transit times (T_c) for HAT-P-32b obtained from separately fitting our seven light curves (Figure 10) and the available data (Hartman et al. 2011) are listed in Table 11. Additional mid-transit times cited from Sada et al. (2012), Gibson et al. (2013), and Seeliger et al. (2014) are also listed in Table 11. We then fit these mid-transit times with a linear function (similar to Equations (1)–(3)), resulting in

$$T_c(N) = 2455867.402743(49) + N \times 2.15000820(13). \quad (4)$$

The quantities in the parentheses represent the uncertainties in the final digit of the preceding number. The orbital ephemeris agrees well with the results from Seeliger et al. (2014).

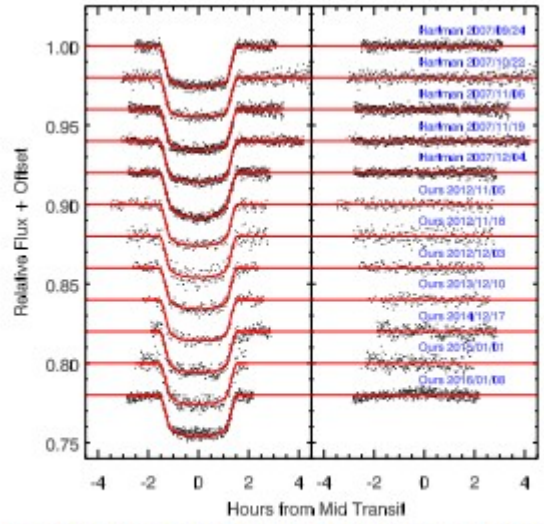

Figure 10. Seven new transit light curves and five previously published light curves (Hartman et al. 2011) for HAT-P-32b. Best-fitting models are shown with red lines in the left panel, and the residuals to the fit are shown in the right.

Figure 11 shows that the deviations of the mid-transit times from the refined orbital ephemeris are small, with an rms of 31 s. A detailed TTV study for HAT-P-32b has been conducted by Seeliger et al. (2014), who analyzed a total of 29 mid-transit times (shown by green points in Figure 10), and excluded TTVs with amplitudes larger than 1.5 minutes. Our results based on the new data shown by the red points are consistent with their conclusion. An upper mass limit of a potential perturber in the HAT-P-32b system will be presented in Section 4.3.

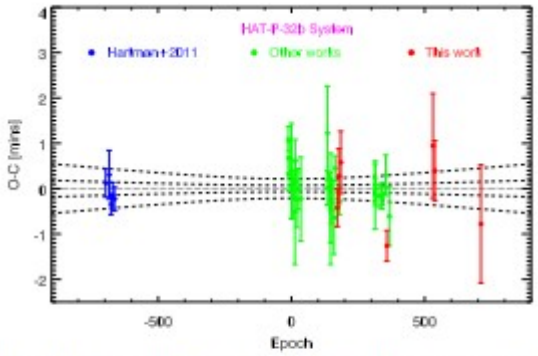

Figure 11. Same as Figure 9, but for HAT-P-32b. The red and blue points represent the mid-transit times obtained from our fits based on our light curves and the published data in Hartman et al. (2011), respectively, while the green points are the mid-transit times cited from Sada et al. (2012), Gibson et al. (2013), and Seeliger et al. (2014). Most of the mid-transit times show good agreement with the refined ephemeris (see Equation (4)) at the $\pm 3\sigma$ level, giving an rms scatter of 31 s.

4.2.3. HAT-P-36b

We used the exact same technique as that used in Sections 4.2.1 and 4.2.2 to update the orbital ephemeris and to analyze the TTVs for HAT-P-36b. The separate fits were applied on each of our 26 light curves and the published data from Bakos et al. (2012) and Mancini et al. (2015). The best-fitting models for each light curve are plotted in Figure 12. The resulting mid-transit times are listed in Table 12. The updated transit ephemeris is

$$T_c(N) = 2456698.735910(149) + N \times 1.32734660(33). \quad (5)$$

The quantities in the parentheses represent the uncertainties in the final digit of the preceding number. Our orbital ephemeris agrees well with the result from Bakos et al. (2012) and Mancini et al. (2015).

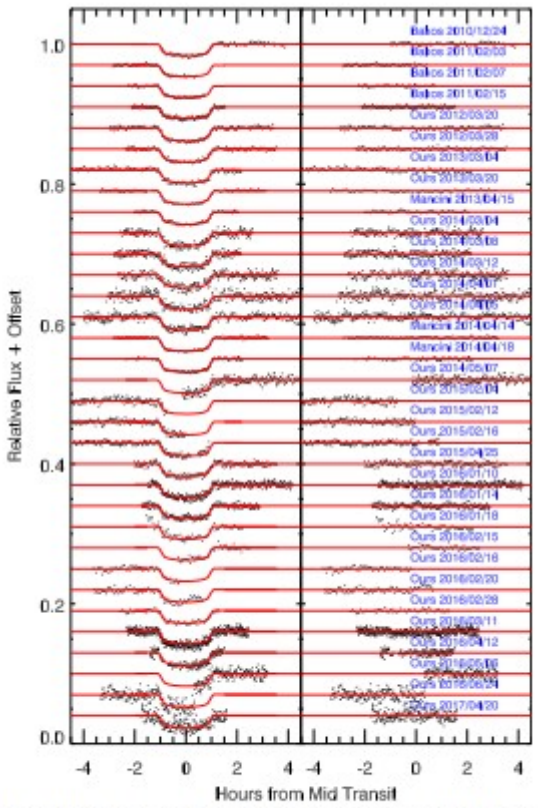

Figure 12. Twenty-six new transit light curves and seven published light curves (Bakos et al. 2012; Mancini et al. 2015) for HAT-P-36b. Best-fitting models are shown with red lines in the left panel, and the residuals to the fit are shown in the right.

Figure 13 shows the deviations of mid-transit times from the new orbital ephemeris for HAT-P-36b, giving an rms of 71 s. Although the follow-up time span and quantity for HAT-P-36b are significantly extended, no obvious TTV signal is detected. Similar to the HAT-P-9b and HAT-P-32b systems, an upper mass limit on a potential perturber in this system is placed in Section 4.3.

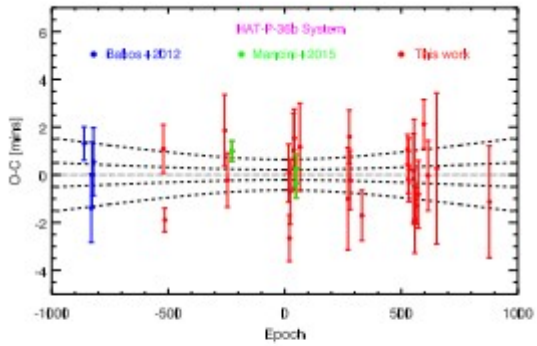

Figure 13. Same as Figure 9, but for HAT-P-36b. The blue and green points represent mid-transit times obtained from our fits based on the published light curves from Bakos et al. (2012) and Mancini et al. (2015), respectively, while the red points represent these obtained with our photometric data. Most of the mid-transit times are consistent with the refined ephemeris (see Equation (5)) at the $\pm 3\sigma$ level, giving an rms scatter of 71 s.

4.3. Orbital Stability and Mass Limits of Additional Perturbers

The results from our mid-transit time study (see Section 4.2) allow us to infer an upper mass limit for an additional planet in each system. A perturbing planet will introduce a change in the mid-transit times of a known planet, which can be quantified by the rms scatter around the nominal (unperturbed) linear ephemeris. The TTV effect is amplified for orbital configurations involving mean-motion resonances (Agol et al. 2005; Holman & Murray 2005; Nesvorný & Morbidelli 2008). In principle, this amplification would allow for the detection of low-mass planetary perturbers. A larger perturbation implies a larger scatter around the nominal ephemeris.

The calculation of an upper mass limit is performed numerically via direct orbit integrations. For this task, we have modified the fortran-based MICROFARM[15] package (Goździewski 2003; Goździewski et al. 2008) which utilizes OpenMPI[16] to spawn hundreds of single-task parallel jobs on a suitable super-computing facility. The package's main purpose is the numerical computation of the Mean Exponential Growth factor of Nearby Orbits (MEGNO; Cincotta & Simó 2000; Goździewski et al. 2001; Cincotta et al. 2003) over a grid of initial values of orbital parameters for an n-body problem. The calculation of the rms scatter of TTVs in the present work follows a direct brute-force method, which proved to be robust given the availability of computing power.

Within the framework of the three-body problem, we integrated the orbits of one of our three hot Jupiters and an additional perturbing planet around a central mass. The mid-transit time was calculated iteratively to a high precision from a series of back-and-forth integrations once a transit of the transiting planet was detected. The best-fit radii of both the planet and the host star were accounted for. We then calculated an analytic least-squares regression to the time series of transit numbers and mid-transit times to determine a best-fitting linear ephemeris with an associated rms statistic for the TTVs. The rms statistic was based on a 20-year integration corresponding to 1864 transits for HAT-P-9b, 3398 transits for HAT-P-32b, and 5505 transit events for HAT-P-36b. This procedure was then applied to a grid of masses and semimajor axes of the perturbing planet while fixing all of the other orbital parameters. In this study, we have chosen to start the perturbing planet on a circular orbit that is coplanar with the transiting planet; this implies that $\Omega_2 = 0°$ and $\omega_2 = 0°$ for the perturbing planet. This setting provides the most conservative estimate of the upper mass limit of a possible perturber (Bean 2009; Fukui et al. 2011; Hoyer et al. 2011, 2012). For the interested readers, we refer to Wang et al. (2018d), which has studied the effects of TTVs on varying initial orbital parameters.

In order to calculate the location of mean-motion resonances, we have used the same code to calculate MEGNO on the same parameter grid. However, this time we integrated each initial grid point for 1000 yr, allowing this study to highlight the location of weak chaotic high-order mean-motion

resonances. In short, MEGNO quantitatively measures the degree of stochastic behavior of a nonlinear dynamical system and has been proven useful in the detection of chaotic resonances (Goździewski et al. 2001; Hinse et al. 2010). In addition to the Newtonian equations of motion, the associated variational equations of motion are solved simultaneously, allowing the calculation of MEGNO at each integration time step. The MICROFARM package implements the ODEX[17] extrapolation algorithm to numerically solve the system of first-order differential equations.

Following the definition of MEGNO (denoted as $\langle Y \rangle$; Cincotta & Simó 2000), in a dynamical system that evolves quasi-periodically, the quantity $\langle Y \rangle$ will asymptotically approach 2.0 for $t \to \infty$. In that case, often the orbital elements associated with that orbit are bounded. In case of a chaotic time evolution, the $\langle Y \rangle$ diverges away from 2.0 with orbital parameters exhibiting erratic temporal excursions.

Importantly, MEGNO is unable to prove that a dynamical system is evolving quasi-periodically, meaning that a given system cannot be proven to be stable or bounded for all of the times. The integration of the equations of motion only considers a limited time period. However, once a given initial condition has found to be chaotic, there is no doubt about its erratic nature in the future.

In the following, we will present the results of each system for which we have calculated the scatter of TTVs on a grid of the masses and semimajor axes of a perturbing planet in a circular, coplanar orbit. The results are shown in Figures 14–16 with a resolution of 1024 × 500 pixels. In each of the three cases, we find the usual instability region located in the proximity of the transiting planet with MEGNO color coded as yellow (corresponding to $\langle Y \rangle > 5$). The extent of this region coincides with the results presented in Barnes & Greenberg (2006).

The perturbing planet was always started on a circular orbit with the same orbital orientation as the transiting planet. If there is an additional planet in the system, we think it is reasonable for the two planets to share the same orbital plane. The assumption on the orbital shape of the perturber is somewhat arbitrary. We refer the reader to Wang et al. (2018d) for an exploration of the effects of starting the perturbing planet on a higher eccentricity orbit.

For the HAT-P-9b system, the considered initial conditions seem to render the $P_2/P_1 = 1/1$ co-orbital resonance to be stable/quasi-periodic. In comparison, this is not the case for the other two systems. In each map, we mark the locations of several mean-motion resonances with arrows. By overplotting the rms scatter of the mid-transit times for a certain value, we find that the TTVs are relatively more sensitive at orbital architectures involving mean-motion resonances, confirming the results by Agol et al. (2005) and Holman & Murray (2005). As shown in Figure 14, we find that a

perturber of mass (upper limit) around 1 $M_{\oplus}$ will produce an rms of 131 s when located in the P_2/P_1 = 2:1, 5:2, and 3:1 exterior resonance. For the 1:2 interior resonance, a perturber mass (upper limit) as small as 0.15 $M_{\oplus}$ could also generate a mid-transit time scatter of 131 s.

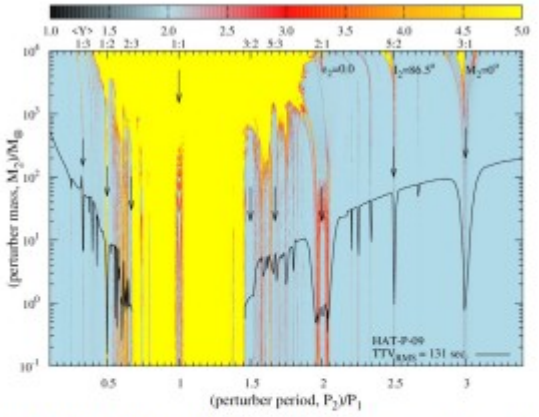

Figure 14. MEGNO ($\langle Y \rangle$) stability map for the HAT-P-9b system. We overplot the map with an upper mass of a hypothetical perturbing planet introducing a mid-transit time rms scatter of 131 s (solid line) as obtained in this study. For initial conditions resulting in a quasi-periodic (i.e., bounded) motion of the system, the $\langle Y \rangle$ value is close to 2.0 (color coded blue). For chaotic (i.e., unstable) motion, the $\langle Y \rangle$ is diverging away from 2.0 (color coded red to yellow). Vertical arrows indicate (P_2/P_1) orbital resonances between the perturber and the transiting planet. The two planets were assumed to be coplanar, and the eccentricity of the perturbing planet was initially set to zero.

For the HAT-P-32b system, a perturbing planet with an upper mass limit in the range 0.1 to 1 $M_{\oplus}$ could theoretically cause a mid-transit time scatter of 31 s when located in a 1:4, 1:3, 1:2 (interior) or 2:1, 9:4, 7:3, 5:2, 8:3, 3:1, 7:2, or 4:1 (exterior) orbital resonance. This is seen from Figure 15.

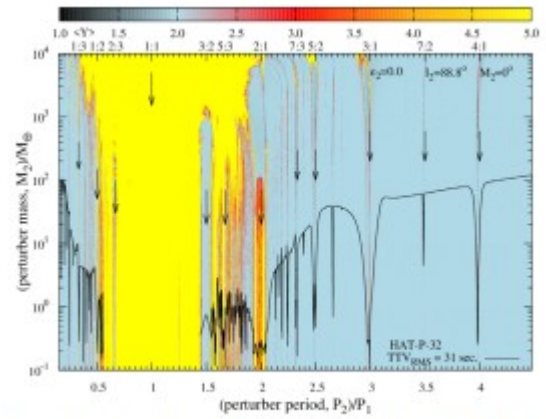

Figure 15. Same as Figure 14, but this time considering the HAT-P-32b system. The solid line is for TTVs with an rms scatter of 31 s.

For the HAT-P-36b system, the result is somewhat more complex, and we refer to Figure 16. For the majority of the aforementioned orbital resonance configurations, a mid-transit time scatter of 71 s is produced by a perturber with an upper mass in the range of 1–10 $M_{\oplus}$. The exception is the 1:2 interior resonance, for which we find that an upper mass limit of 0.3 $M_{\oplus}$ can produce the same scatter.

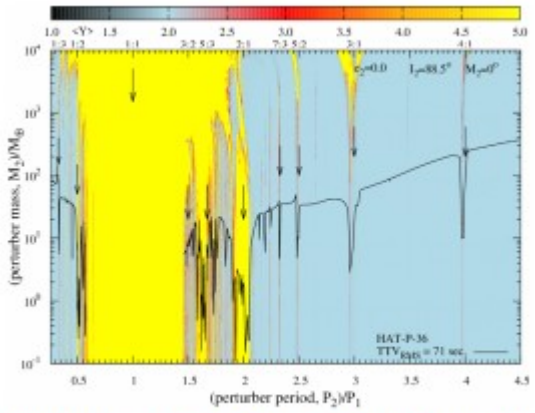

Figure 16. Same as Figure 14, but this time considering the HAT-P-36b system. The solid line is for TTVs with an rms scatter of 71 s.

These observations provide accurate anchors for searches for transit time variations with the ongoing *Transiting Exoplanet Survey Satellite* (*TESS)* mission (Ricker et al. 2015), which will complete and follow up almost all transiting hot Jupiters orbiting bright stars (Wang et al. 2019).

5. Summary and Conclusions

The TEMP aims to further understand planetary interior structures, formation, and evolution with long-term high-precision photometric follow-up observations (Wang et al. 2017a, 2017b, 2018b).

As the initial targets for TEMP, the HAT-P-9b, HAT-P-32b, and HAT-P-36b systems have been observed six, seven, and twenty-six times from 2012 March to 2017 April with three telescopes in China and South Korea.

In this work, we have performed a global fit for each system based on both our new photometric observations and previously published RV data to revisit the fundamental system parameters. The system parameters we found show excellent agreement with those of previous studies, except the R_P/R_* for HAT-P-36b. The value of R_P/R_* from our R-band data is larger than the published i-band value (Bakos et al. 2012) at the 4.5σ level.

Based on the obtained system parameters, we performed separate fits for all of the light curves to get precise mid-transit times. With these mid-transit times in hand, we refined the orbital ephemeris for each system. In comparison to the published results, our ephemerides are more precise and reliable as the result of more high-precision transits that greatly expand the total time spans of observations.

We have also performed TTV analyses for these three systems. Because no significant TTV signals were found, we put upper mass limits on potential close-in planetary companions.

For the HAT-P-9b system, a perturber with mass (upper limit) around 1 $M_\oplus$ will produce TTVs with the rms of 131 s at the P_2/P_1= 2:1, 5:2, or 3:1 exterior resonances. For the 1:2 interior resonance, the mass can be as small as 0.15 $M_\oplus$.

For the HAT-P-32b system, we constrained the upper mass of a perturber in the range of 0.1 to 1 $M_{\oplus}$ at the 1:4, 1:3, 1:2 (interior) or 2:1, 9:4, 7:3, 5:2, 8:3, 3:1, 7:2, or 4:1 (exterior) orbital resonances, with the given rms scatter of 31 s.

For the HAT-P-36b system, the upper mass of a perturber is constrained to the range of 1–10 $M_{\oplus}$ for most of the aforementioned orbital resonance configurations with the rms scatter of 71 s. But for the 1:2 interior resonance, a perturber with a mass of 0.3 $M_{\oplus}$ can also produce the same rms scatter.

These observations provide accurate anchors for future searches for TTVs with the ongoing *TESS* mission (Ricker et al. 2015), which will largely complete the sample of transiting hot Jupiters orbiting bright stars (Wang et al. 2019).

This research is supported by the National Basic Research Program of China (Nos. 2013CB834902 and 2014CB845704), the National Natural Science Foundation of China (under grant Nos. 11433005, 11673027, 11373033, 11503009, 11333002, and 11673011), and the National Defense Science and Engineering Bureau civil spaceflight advanced research project (D030201). We acknowledge the support of the staff of the Xinglong 60 cm telescope. This work was partially supported by the Open Project Program of the Key Laboratory of Optical Astronomy, National Astronomical Observatories, Chinese Academy of Sciences. S.W. thanks the Heising-Simons Foundation for the generous support. A.B.D. is supported by the National Science Foundation Graduate Research Fellowship Program under grant No. DGE-1122492. T.C.H. acknowledges KASI research grant 2016-1-832-01 and 2017-1-830-03. Numerical computations were partly carried out using the KASI (polaris) High-performance Computing cluster at KASI/South Korea.

Facilities: Beijing: Schmidt - , Beijing: 0.6 m - .

Software: SExtractor (Bertin & Arnouts 1996), EXOFAST (Eastman et al. 2013), JKTEBOP (Southworth 2008).

Footnotes

13 Online procedure available at http://astroutils.astronomy.ohio-state.edu/exofast/exofast.shtml.

14 http://www.astro.keele.ac.uk/jkt/codes/jktebop.html.

15 https://bitbucket.org/chdianthus/microfarm/src

16 https://www.open-mpi.org

17 https://www.unige.ch/~hairer/prog/nonstiff/odex.f

References

Agol E., Steffen J., Sari R. and Clarkson W. 2005 MNRAS 359 567

Bakos G., Noyes R. W., Kovács G. et al 2004 PASP 116 266

Bakos G. Á., Csubry Z., Penev K. et al 2013 PASP 125 154

Bakos G. Á., Hartman J. D., Torres G. et al 2012 AJ 144 19

Barnes R. and Greenberg R. 2006 ApJL 647 L163

Bean J. L. 2009 A&A 506 369

Bean J. L., Miller-Ricci Kempton E. and Homeier D. 2010 Natur 468 669

Becker J. C., Vanderburg A., Adams F. C., Rappaport S. A. and Schwengeler H. M. 2015 ApJL 812 L18

Bertin E. and Arnouts S. 1996 A&AS 117 393

Cincotta P. M., Giordano C. M. and Simó C. 2003 PhyD 182 151

Cincotta P. M. and Simó C. 2000 A&AS 147 205

Claret A. and Bloemen S. 2011 A&A 529 A75

Dittmann J. A., Close L. M., Scuderi L. J., Turner J. and Stephenson P. C. 2012 NewA 17 438

Eastman J., Gaudi B. S. and Agol E. 2013 PASP 125 83

Eastman J., Siverd R. and Gaudi B. S. 2010 PASP 122 935

Fukui A., Narita N., Tristram P. J. et al 2011 PASJ 63 287

Gibson N. P., Aigrain S., Barstow J. K. et al 2013 MNRAS 436 2974

Gillon M., Triaud A. H. M. J., Fortney J. J. et al 2012 A&A 542 A4

Gómez Maqueo Chew Y., Faedi F., Cargile P. et al 2013 ApJ 768 79

Goździewski K. 2003 A&A 398 1151

Goździewski K., Bois E., Maciejewski A. J. and Kiseleva-Eggleton L. 2001 A&A 378 569

Goździewski K., Breiter S. and Brczyk W. 2008 MNRAS 383 898

Hartman J. D., Bakos G. Á., Torres G. et al 2011 ApJ 742 59

Hinse T. C., Christou A. A., Alvarellos J. L. A. and Goździewski K. 2010 MNRAS 404 837

Hinse T. C., Han W., Yoon J.-N. et al 2015 JASS 32 21

Holman M. J. and Murray N. W. 2005 Sci 307 1288

Holman M. J., Winn J. N., Latham D. W. et al 2006 ApJ 652 1715

Hoyer S., Rojo P., López-Morales M. et al 2011 ApJ 733 53

Hoyer S., Rojo P. and López-Morales M. 2012 ApJ 748 22

Huang C., Wu Y. and Triaud A. H. M. J. 2016 ApJ 825 98

Kim C.-H., Song M.-H., Yoon J.-N., Han W. and Jeong M.-J. 2014 ApJ 788 134

Knutson H. A., Fulton B. J., Montet B. T. et al 2014 ApJ 785 126
Mancini L., Esposito M., Covino E. et al 2015 A&A 579 A136
Mancini L., Southworth J., Ciceri S. et al 2013 A&A 551 A11
Millholland S., Wang S. and Laughlin G. 2016 ApJL 823 L7
Nascimbeni V., Piotto G., Bedin L. R. and Damasso M. 2011 A&A 527 A85
Nesvorný D. and Morbidelli A. 2008 ApJ 688 636
Pepper J., Pogge R. W., DePoy D. L. et al 2007 PASP 119 923
Pollacco D. L., Skillen I., Collier Cameron A. et al 2006 PASP 118 1407
Raetz S., Maciejewski G., Seeliger M. et al 2015 MNRAS 451 4139
Ricker G. R., Winn J. N., Vanderspek R. et al 2015 JATIS 1 014003
Sada P. V., Deming D., Jennings D. E. et al 2012 PASP 124 212
Seeliger M., Dimitrov D., Kjurkchieva D. et al 2014 MNRAS 441 304
Shporer A., Bakos G. Á., Bouchy F. et al 2009a ApJ 690 1393
Shporer A., Mazeh T., Pont F. et al 2009b ApJ 694 1559
Sing D. K., Fortney J. J., Nikolov N. et al 2016 Natur 529 59
Sing D. K., Wakeford H. R., Showman A. P. et al 2015 MNRAS 446 2428
Southworth J. 2008 MNRAS 386 1644
Southworth J. 2012 MNRAS 426 1291
Southworth J., Hinse T. C., Jørgensen U. G. et al 2009 MNRAS 396 1023
Southworth J., Maxted P. F. L. and Smalley B. 2004 MNRAS 351 1277
Steffen J. H., Ragozzine D., Fabrycky D. C. et al 2012 PNAS 109 7982
Wang S., Addison B., Fischer D. A. et al 2018a AJ 155 70
Wang S., Jones M., Shporer A. et al 2019 AJ 157 51
Wang S., Wang X.-Y., Wang Y.-H. et al 2018b AJ 156 181
Wang S., Wu D.-H., Addison B. C. et al 2018c AJ 155 73
Wang S., Wu D.-H., Barclay T. and Laughlin G. P. 2017a arXiv:1704.04290
Wang S., Zhang H., Zhou J.-L. et al 2014 ApJS 211 26
Wang X.-Y., Wang S., Hinse T. C. et al 2018d PASP 130 064401
Wang Y.-H., Wang S., Liu H.-G. et al 2017b AJ 154 49
Winn J. N. and Fabrycky D. C. 2015 ARA&A 53 409
Zhou X., Chen J., Xu W. et al 1999 PASP 111 909
Zhou X., Jiang Z.-J., Xue S.-J. et al 2001 ChJAA 1 372